

AC_VS/AS19_01 Report

Validation Study of GOME-2 SIF with GOSAT/OCO-2 SIF, MPI-BGC NIRv and Flux-tower GPP. Using NIRv to bridge the gap of spatial representativity.



Document Type	SAF/AC/KNMI/RP
Issue	1.0
Date	30-04-2020
Number of Pages	24
Affiliated Institute	KNMI
Summary contents	Final report of the AC_VS/AS19_01 visiting scientist activity
Period	1 Nov 2019 - 31 Mar 2020
Authors	Anteneh G. Mengistu
Contributors	Maurits L. Kooreman (KNMI), Wouter Peters (WUR), Gerbrand Koren (WUR) Olaf N. E. Tuinder (KNMI), K. Folkert Boersma (KNMI/WUR)

Contents

1	Introduction	1
2	Data and Methods	3
2.1	SIF Data	3
2.2	Gridded data sets	4
2.3	Eddy Covariance Tower Data	4
2.4	Method	5
3	Results and Discussions	8
3.1	Inter-satellite SIF comparison	8
3.2	Inter-comparison at ecosystem level	11
3.3	Comparison of SIFTER with OCO-2 SIF and EC GPP	14
3.4	Comparison SIFTER with NIRv and EC GPP	15
4	Conclusions	17

Abstract

Sun-Induced chlorophyll Fluorescence (SIF) retrievals provide a new perspective for monitoring vegetation photosynthesis from space and these data is increasingly used to estimate Gross Primary Productivity (GPP). Accurate estimation of GPP plays an important role in the carbon budget in the context of global change. The Royal Netherlands Meteorological Institute (KNMI) and Wageningen University and Research (WUR) retrieve a mid-morning (9:30 local time) SIF values from the GOME-2 sensor on the MetOp satellite series, based on the improved SIFTER algorithm [SIFTER v2; van Schaik et al., 2020]. Here we assess the quality of this new product by comparison to independent SIF, Near-Infrared Reflectance of vegetation (NIRv) and GPP products from other satellite, model and ground-based platforms, both at a global and ecosystem scale. This validation study is part of the Operational Readiness Review for the SIFTER product development within the EUMETSAT SAF network. The new SIFTER v2 has a good agreement with the global distribution of NIRv, GPP from Max Planck Institute of Biogeochemistry (MPI-BGC) and SIF from Orbiting Carbon Observatory 2 (OCO-2). The spatial and temporal patterns of the retrieved SIFTER also agree well with the global GPP patterns from MPI-BGC. The inter-annual mean SIFTER v2 has a strong spatial correlation (0.76 - 0.93) with OCO-2 SIF, (0.86 - 0.97) with NIRv in the years 2015-2018 and (0.69 - 0.92) with MPI-BGC GPP [Jung et al., 2011] covering the period from 2007-2011 in capturing the latitudinal distribution over three different latitudinal zones. SIFTER v2 also shows excellent skill in capturing seasonal patterns of NIRv, OCO-2 SIF and GPP over different regions across the globe with correlation ranging from 0.62 to 0.99. SIFTER shows a better agreement with NIRv and OCO-2 SIF than with MPI-BGC GPP both in capturing the latitudinal and seasonal variabilities. Unlike OCO-2 SIF and NIRv, SIFTER shows a significant reduction in productivity during the dry months of the tropical regions. Moderate relationships among the datasets were found in tropical rainforest regions and low productivity areas in their seasonal cycle. Furthermore, we evaluate the relation between SIFTER v2, OCO-2 SIF and EC GPP at ecosystem level in a $1^\circ \times 1^\circ$ boxes around five EC flux towers. Monthly mean correlation results vary from strong to weak depending on surrounding biome type. Generally, more homogeneous regions show a stronger correlation than heterogeneous land cover regions. A down-scaled high resolution (0.05°) of SIFTER and NIRv show a better relationship with the EC GPP than the coarse resolution (0.5°).

Chapter 1

Introduction

Terrestrial gross primary production (GPP), the amount of carbon absorbed by terrestrial plants via photosynthesis, constitutes the largest CO₂ flux between the terrestrial biosphere and the atmosphere [Quéré et al., 2015]. The lack of a reliable GPP proxy with sufficient resolution and global coverage makes it the most uncertain in the carbon budget study. For that reason, many national and international organizations have put efforts into acquiring the most reliable GPP estimates with good spatio-temporal resolution that can be used for global and regional studies. The most reliable GPP estimates arguably comes from the Eddy Covariance (EC) techniques, performed by instruments usually mounted on towers. The EC technique is a well-established method to directly measure flux over a fetch larger than typical plot-level measurements [Baldocchi, 2003]. EC provides direct measurements of forest-atmosphere exchanges such as carbon dioxide, water, energy, and other trace gases and allow us to observe whole-ecosystem metabolism. However, EC measurements are still very sparse and have a very small footprint of about 2 km [Liu et al., 2012] which limits their use to regional studies. EC techniques provide continuous and high-frequency measurements sufficient to study diurnal, seasonal and interannual variations at the ecosystem level Aubinet et al. [2012].

At the modeling front, the Max Planck Institute of Biogeochemistry and FLUXCOM are notable. Model products have good spatio-temporal coverage but they are highly susceptible to uncertainties due to their background modeling assumptions and uncertainties in the input meteorological data. This fuels the need for GPP estimation from direct measurements that have a higher accuracy and do not rely on other meteorological inputs. Satellites measure light emitted by chlorophyll and bypass through the atmosphere. The absorbed solar radiation has three fates during photosynthesis: (1) It is absorbed by chlorophyll molecules in the leaves and used for generating energy, (2) it is lost as heat energy and (3) a small fraction (1%) is re-emitted as fluorescence at a higher wavelength compared to the absorption [Schlau-Cohen and Berry, 2015]. Sun-Induced Fluorescence (SIF) has a spectrally smooth signature with peaks around 683 (red fluorescence) and 736 nm (far-red fluorescence). Chlorophyll itself re-absorbs fluorescence within the canopy below 700 nm. Photons that escape re-absorption, travel through the atmosphere and can be recorded by space borne sensors. Recent studies show that SIF and Near-Infrared reflectance of vegetation (NIRv) exhibit a strong linear correlation with GPP from model and ground based observations and that they have a strong predictive skill of GPP even without including any climatic or model information [Frankenberg et al., 2011; Zeng et al., 2019; Badgley et al., 2017]. Furthermore, the possibility of inferring GPP from SIF/NIRv at high resolution (0.05° grid) [Duveiller and Cescatti, 2016; Li and Xiao, 2019] provides an exceptional opportunity in the study of land photosynthesis. For this reason, SIF and NIRv get much attention in the study of global and regional estimation of GPP. Most recent satellite missions such as OCO-2, GOSAT, GOME-2, TROPOMI and in the future FLEX, put numerous efforts into inferring GPP from SIF with the goal of creating a global map of biosphere-atmosphere interaction

at high resolution and accuracy.

Remote sensing technologies usually have high spatial coverage with polar-orbiting satellites, while the continuous temporal sampling is generally not possible. From polar-orbiting satellite platforms, we can only get from zero to possibly up to a few observations per day depending on the swath width of the instrument and latitude. Multiple observations per day with a single instrument are only possible at high latitudes and with a wide swath instrument, e.g. [Guanter et al., 2015]. If observing conditions are not favorable, e.g. due to clouds or aerosols, a valid observation may not be present over several days [Sims et al., 2005]. Retrieval of SIF from high spatial resolution of OCO-2 ($1.3 \times 2 \text{ km}^2$) allows a direct comparison with EC measurements. In contrast, due to its smaller swath OCO-2 has a large repeat period which restricts its application in understanding temporal variation in GPP as a monthly mean is restricted to a few data samples. On the other hand, the swath of GOME-2 is so wide (1920 km per orbit) with a coarse spatial resolution ($40 \times 80 \text{ km}^2$) that in principle allows a global coverage of once per 2 days. This allows retrieval of SIF possible at 0.5° grid at monthly resolution with more representative data in each month. OCO-2 may have much smaller pixels, but the coverage is sparse, so at most 1-2 measurements per location per month. In agreement with this hypothesis, Wei et al. [2018] showed the 16-day average values of GOME-2 SIF has a better performance in GPP estimation than OCO-SIF averages. Plants can reflect, transmit, and absorb different portions of the near-infrared radiation. Healthy vegetation will reflect more near-infrared energy than an unhealthy plant. The NIRv which is the product of total measured Near-Infrared radiation and the most commonly used vegetation greenness index (NDVI), shows a strong relation with the global vegetation patterns and strongly correlated with SIF [Badgley et al., 2017]. One of the primary advantages of NIRv is that it can be calculated at higher resolution using existing satellite sensors such as MODerate-resolution Imaging Spectroradiometer (MODIS). Here, we use NIRv from MODIS collection MCD43C4v006 to assess the performance of GOME-2 SIF in comparison to NIRv.

Even if SIF is more or less a direct measurement of photosynthesis the relation is neither unique nor simple as it is subject to different retrieval techniques. Particularly, the challenge is associated with dismantling the SIF contribution from the measured radiances, which are mostly composed of reflected sunlight with SIF adding only a small amount, typically less than 1%. Following, a similar statistical approach as Joiner et al. [2013], The Royal Netherlands Meteorological Institute (KNMI) developed SIF retrieval code with some fundamentally different choices called SIFTER [Sanders et al., 2016; van Schaik et al., 2020]. van Schaik et al. [2020] evaluates the retrieval algorithm, product, and uncertainties of SIFTER v2 against GOME-2 SIF from Joiner et al. [2013]. But the SIFTER v2 has not yet been validated against ground-based data or other sensors. Therefore, it is worth to assess the performance of this new product with the known most accurate independent SIF product from other satellites and also with GPP from model and EC technique before utilizing the data to elucidate the photosynthetic activity of the biosphere. In addition, an inter-comparison with independent satellite and model products will give much more confidence in the product for global and large scale studies. In this validation study, we identify spatio-temporal similarity and “dissimilarity” between level-2 SIF products of KNMI with independent SIF products from OCO-2, Near-Infrared reflectance of vegetation and GPP from the MPI-BGC. We also use eddy flux data from five towers in different geographical regions and with different biome types to assess the level of agreement between SIFTER and Eddy covariance GPP at the ecosystem level.

Chapter 2

Data and Methods

2.1 SIF Data

The Global Ozone Monitoring Experiment-2 [Munro et al., 2006] senses the Earth's backscattered radiance and extraterrestrial solar irradiance. It is a nadir-scanning medium-resolution (~ 0.5 nm) spectrometer that operates between 240 and 790 nm in four detector channels. Currently, there are three GOME-2 instruments operating onboard EUMETSAT's polar-orbiting Meteorological Operational Satellites (MetOp-A, -B and -C) launched on respectively 19 October 2006, 17 September 2012 and 7 November 2018. These sun-synchronous polar orbit satellites fly at an altitude of approximately 820 km and have an equator crossing (descending node) around 09:30 equator crossing local time. The wide spectral range allows GOME-2 to measure a large number of atmospheric trace constituents, with the emphasis on global ozone distributions. The fourth channel in the near-infrared (593 -790 nm) encompasses the SIF wavelength region. The channel has a spectral sampling of approximately 0.2 nm and a spectral resolution of 0.5 nm with a signal-to-noise ratio up to 2000 [Callies et al., 2000]. The large GOME-2 default swath width of 1920 km with a footprint size of 80 x 40 km² enables a global coverage within 1.5 days.

Based on the statistical approaches developed by Joiner et al. [2013], the retrieval code developed at KNMI [Sanders et al., 2016; van Schaik et al., 2020] uses a multi-year dataset of measurements over the non vegetated Sahara to construct the atmospheric reference spectra used to distinguish the small SIF signals from the complex structure of transmittance and reflectance from other atmospheric constituents such as water vapor. Based on the improved algorithm, KNMI estimates the global SIF from GOME-2A covering the period from 2007 to 2020.

For the comparison of this product, we also use SIF products from the Orbiting Carbon Observatory 2 (OCO-2) and the Greenhouse Gases Observing Satellite (GOSAT). These SIF products are independent both in the observation and retrieval processes. We use the SIF lite product version B8100r from OCO-2. This product includes SIF retrieved separately from windows around 757 nm and around 771 nm. These retrievals are made from soundings with a footprint of 1.3 x 2.25 km² at nadir. Hence, SIFTER v2 is retrieved at a different spectral window around 737 nm. To make the comparison of GOME-2 SIFTER v2 and OCO-2 SIF we recalculate the OCO-2 SIF at 740 nm from these two retrievals (SIF at 757 and SIF at 771 nm) using scale factors from leaf-level measurements conducted by Magney et al. [2019] using the following formula:

$$\text{SIF}_{740} = 1.56 * \frac{(\text{SIF}_{757} + 1.8 * \text{SIF}_{771})}{2} \quad (2.1)$$

Table 2.1: Some basic information on the satellites used for the study. *After July 2013, the GOME-2(a) swath is half the size, pixels are 40x40 km² and repeat cycle is increased to 3 days.

	GOME-2	OCO-2	GOSAT
Temporal coverage	01/2007 to present	09/2014 to present	04/2009 to present
Spatial resolution	40 x 80 km ² *	1.3 x 2 km ²	10 km diameter
Equator crossing time	~9:30 hrs	~13:36 hrs	~13:00 hrs
Repeat cycle	1.5 days*	16 days	3 days
Spatial resolution for global monthly mapping	0.5° x 0.5°	1° x 1°	2° x 2°

2.2 Gridded data sets

Monthly average estimation of terrestrial GPP from the Max Planck Institute of Biogeochemistry integration group was used to see how good SIFTER is capturing the spatio-temporal patterns of plant photosynthesis. This GPP product is constructed using a machine learning method to upscale information from flux-towers up to a 0.5° x 0.5° grid, aided by gridded meteorological and remote sensing co-variables described by Jung et al. [2011] and freely accessed from <https://www.bgc-jena.mpg.de/geodb/projects/Data.php>). This product will henceforth be referred to as MPI-BGC GPP.

The NIR_v represents the fraction of reflected Near-Infrared reflectance (NIR) of light that originates from vegetation. NIR_v was first described as a proxy for photosynthesis by Badgley et al. [2017]. More accurate retrievals of the contribution of vegetation to observed NIR reflectance under a wide array of field conditions, including over sparse canopies and regardless of soil brightness, recent studies use NIR_v for vegetation productivity and computing a NIR_v based SIF at 760 nm [Badgley et al., 2017; Zeng et al., 2019]. In this study we used NIR_v at a spatial resolution of 0.5×0.5 and a monthly temporal resolution for the years 2007-2018. We also used NIR_v at a higher resolution (0.05×0.05, monthly). NIR_v data used here were calculated from gridded MODIS surface reflectance data [Schaaf and Wang, 2015]. NIR_v and SIF are strongly related measurable fluxes as both jointly depend on the flux of the fractional Reflectance of vegetation, incoming solar radiation, and photons that escape from the canopy [Zeng et al., 2019].

2.3 Eddy Covariance Tower Data

To assess the level of agreement of the SIFTER product for different vegetation types across the globe, we collect in situ GPP records from five Eddy Covariance (EC) flux towers across the globe as indicated by the black markers in Fig. 2.1. Flux towers are selected for their representativeness of different biomes and climate conditions. For this study, we chose flux towers at the Morgans Monroe site US-MMS in the Northern Hemisphere forest in the USA, Selhausen Juelich DE-RuS from crop land in Europe, Santarem forest BR-Sa1 from evergreen forest in Brazil, Skukuza ZA-Kru from tropical savanna area in Africa and Sturt Plains AU-Stp from Australian grass land. Details about these locations are presented in table 2.2. Figure 2.1 shows the major land cover classification based on high resolution (0.05°) products of the MODerate-resolution Imaging Spectroradiometer (MODIS) land cover database (MCD12C1). The bottom panels in figure 2.1 show a zoom in of the surrounding land cover vegetation of each tower in a 1° x 1° window centered around the flux tower location (black marker). These panels shows the major vegetation and land heterogeneity around the flux

towers. We use GPP products from daytime partitioning of fluxes (GPP_DT_VUT_REF which is "Gross Primary Production, from Daytime partitioning method, reference selected from GPP versions using model efficiency (MEF). The MEF analysis is repeated for each time aggregation") from the Tair 2 FLUXNET2015 synthesis [DAAC, 2011], OzFlux [Isaac et al., 2017], and the Integrated Carbon Observation System (ICOS), a European Research Infrastructure [ICOS, 2019].

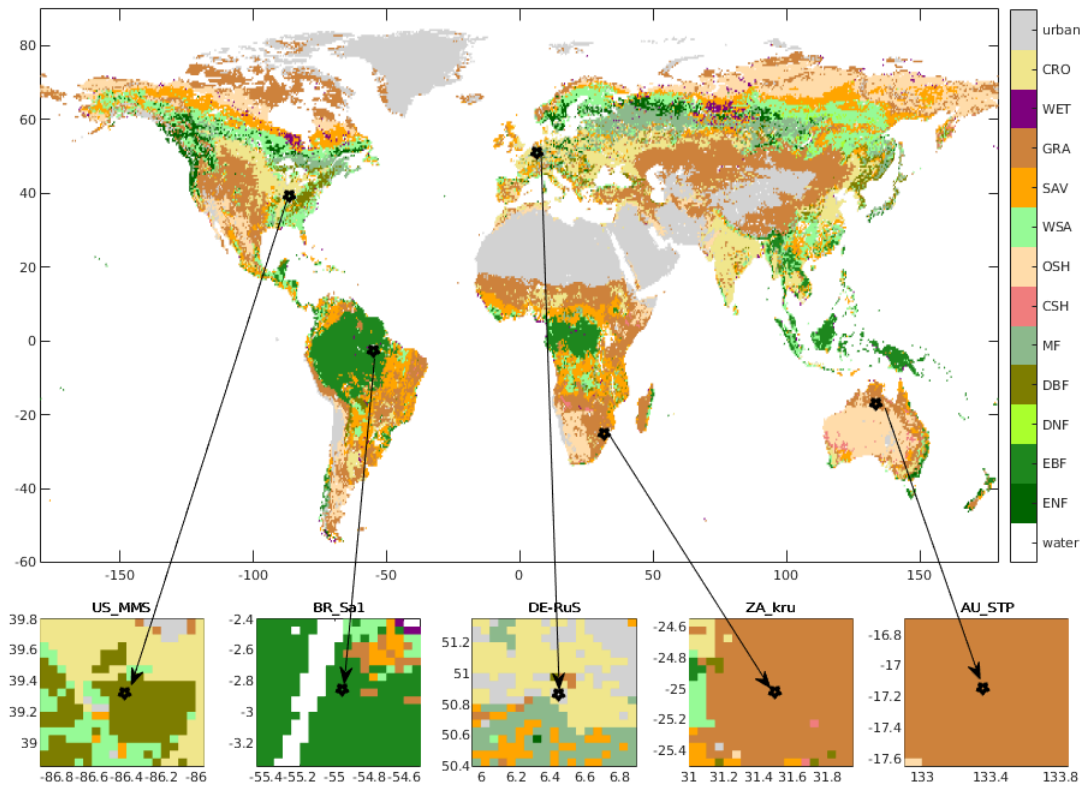


Figure 2.1: The location and vegetation type of eddy covariance flux towers used in the study. The symbols stand for flux towers. The base map is the Moderate Resolution Imaging Spectroradiometer (MODIS) global land cover classification (MCD12C1), and the dominant land cover types include water, evergreen needle-leaf forests (ENF), evergreen broadleaf forests (EBF), deciduous needle-leaf forests (DNF), deciduous broadleaf forests (DBF), mixed forests (MF), closed shrublands (CSH), open shrublands (OSH), woody savannas (WSA), savannas (SAV), grasslands (GRA), permanent wet land (WET), croplands (CRO), urban and built-up (urban), and barren or sparsely vegetated (barren). The bottom panels show the vegetation type in a $1^\circ \times 1^\circ$ grid surrounding the flux towers, indicated by black markers.

2.4 Method

To assess the skill of the SIFTER retrieval of from GOME-2A in capturing the global distribution of SIF and GPP from these independent sources. We look at a global map of SIF from OCO-2 monthly aggregated on

Table 2.2: Information on flux-tower sites. * indicates flux observations before 2007 are available from the towers but we didn't use them in this study.

Site_ID	Site_Name	Country	Veg. Type	Lat. (°N)	Lon. (°E)	Period
AU-Stp	Sturt Plains	Australia	GRA	-17.15	133.35	01-'08 12-'18
BR-Sa1	Santarem-Km67-Primary For.	Brazil	EBF	-2.86	-54.96	01-'00* 12-'11
DE-RuS	Selhausen Juelich	Germany	CRO	50.87	6.45	01-'11 12-'14
US-MMS	Morgan Monroe State For.	USA	DBF	39.32	-86.41	01-'99* 12-'17
ZA-Kru	Skukuza	South Africa	SAV	-25.02	31.50	01-'00* 12-'13

a $1^\circ \times 1^\circ$ grid and GOME-2 monthly aggregated on a $0.5^\circ \times 0.5^\circ$ grid and monthly aggregated NIRv in $0.5^\circ \times 0.5^\circ$ grid covering the period from 2015-2018 as well a multiyear MPI-BGC GPP [Beer et al., 2010]. For the data aggregation, we calculated the mean of each sounding following the quality check instructions as recommended for each retrieval. We also remove SIF retrievals above 70° solar zenith angle. These datasets also used to compare how SIFTER agree with the other datasets in capturing the zonal latitudinal distribution and seasonal patterns at continental scale. Since OCO-2 and MPI-BGC GPP have no overlapping time we look at the inter-comparison of seasonal and climatological scales ignoring the inter-annual fluctuation.

For the inter-comparison of SIF, we evaluated the SIFTER L2 product from GOME-2 against independent SIF datasets from OCO-2 covering the period from September 2014 to December 2018 (after the GOME-2 pixel is changed to $40 \times 40 \text{ km}^2$). For the spatio-temporal coincidence criteria, we use the GOME-2 footprint and compute the spatial mean of OCO-2 SIF recalculated at 740 nm (Eq. 2.1) in a 4-hour interval from the time of GOME-2 observation in the region of each tower. The 4 hour time difference is due to the difference in their local overpass time (see Table 2.1). A scatter plot of OCO-SIF verses SIFTER and preformed a regression analysis to shows the agreement between these dataset. Hence, measurement of SIF from each satellite comes with a certain level of uncertainty we use a reduced major axis regression (RMA) to account for these errors in the fit. The RMA minimizes collective distance between data points and the line by considering a hypotenuse of a right triangle that have two sides parallel to the axes, each side being proportional in length to the standard deviation of each variable [Kilmer and Rodríguez, 2017], and the linear model that it yields is known as the reduced major axis [Carr, 2012]. RMA regression, allows for measurement error in both axes, it assumes that each variable has an error proportional to its standard deviation [Clarke, 1980; Kilmer and Rodríguez, 2017]. The slope of the line will be used to determine whether the two datasets are isometric or whether one of them shows positive or negative allometry [Friedman et al., 2013].

To assess the agreement between SIFTER and GPP at the ecosystem level. We use hourly averaged eddy covariance GPP data computed from the original half-hourly data. OCO-2 SIF at 740 nm and SIFTER were compared to EC GPP averaged at the overpass time of each satellites. We also use the monthly products of EC-GPP to show the skill of SIFTER in capturing the seasonal dynamics of vegetation productivity. Each valid measurement and good quality gap-filled data from the tower was monthly averaged from the original half-hourly EC-GPP from each flux towers within the 1 hr time interval of the overpass time of the satellites and compared the results with both fine and coarse resolution SIFTER and NIRv. To match the EC GPP, which is about 1 km^2 footprint, we developed a scale conversion coefficient for the 0.5° grid cells of the SIFTER by using the NIRv ratio. This method had been also applied in the work of Wei et al. [2018]. The fine resolution SIFTER was created using the ratio of the 0.05° NIRv to the 0.5° NIRv grid cell as a scale factor to account the difference caused by the land heterogeneity. These scale factors shows seasonal variation with a mean of 0.97 ± 0.21 , 1.22 ± 0.07 , 0.83 ± 0.12 , 1.25 ± 0.33 , 1.01 ± 0.15 around AU-Stp, BR-Sa1, DE-RuS, US-

MMS and ZA-Kru respectively. Smallest variance was found around the BR-Sa1 where vegetation cover of the region expected to see less seasonal variability than the other sites. The resulting product is a calculated spatio-temporal SIFTER at a 0.05° and is henceforth referred to as SIF* to distinguish it from the original SIFTER signal.

Chapter 3

Results and Discussions

3.1 Inter-satellite SIF comparison

The four years (2015-2018) average of SIF from GOME-2 only quality-controlled retrievals are gridded at a monthly temporal and on $0.5^\circ \times 0.5^\circ$ grid exhibits the expected spatial vegetation productivity pattern at a global scale (see Fig. 3.1) which is very similar to spatial patterns of SIF from OCO-2 monthly aggregated on $1^\circ \times 1^\circ$ grid, multi-year averages of GPP from MPI-BGC Beer et al. [2010] and NIRv $0.5^\circ \times 0.5^\circ$ grid and NIRv monthly aggregated on $0.5^\circ \times 0.5^\circ$ grid. In general, we observe a fairly good agreement in the global patterns of SIF among these independent satellites and the model estimation of GPP. Highest SIF signal above $1 \text{ mWsr}^{-1}\text{m}^{-2}\text{nm}^{-1}$ was observed in tropical regions like Amazon forest, Ghana, Congo and Indonesia and in some places above 10° north of the equator like in Mexico, Eastern USA, United Kingdom, and China. In contrast, near-zero and negative signals of SIF are observed in deserts like Sahara, Arabian Peninsula, Kalahari, and Patagonian deserts and moderate signals are observed over most parts of Central Europe, Eastern USA, and Southern Asia. Moreover, the global distribution of SIFTER are in good harmony with the GOME-2A SIF retrieval of NASA [Joiner et al., 2013]. The global distribution of SIF between OCO-2 and GOME-2 shows a clear discrepancy in vegetation-free areas such as in Sahara and Arabian peninsula most likely due to greater SIF uncertainty for sparsely vegetated and low productivity regions [Joiner et al., 2016]. We use a multi-year GPP product of MPI-BGC in comparison with annual mean SIF from the satellite soundings and compared them to annual averages of SIF during 2015. SIF is expected to capture seasonal and interannual cycles thereby comparison of SIF and GPP from different years will have a limited effect on the results. This large scale comparison can be considered as a first order fidelity check among these datasets.

The global climatology of SIFTER shows good congruent with general climate and latitudinal variations, indicating the influence of underlying environmental controls on vegetation phenology and productivity are well captured. Fig. 3.2 shows the climatology of zonal mean SIF from these three satellites, NIRv and GPP from MPI-BGC (normalized by dividing with the maximum GPP) during March (top), July (middle) and annual mean (bottom). We split up the latitudinal distribution to three different regions to account for latitudinal distributions in Americas, Africa and Europe, and Oceania and Asia. Fig. 3.2a represents North and South America (longitude from -96° to -25°E). Fig. 3.2b refers to the latitudinal distribution in a longitude range, between -25°E and 55°E , to account for Europe and Africa. Fig. 3.2c represents Asia and Australia for longitudes greater than 55°E . Overall, the latitudinal distribution shows multiple maxima, a larger maximum near the equator as a result of large productivity from the equatorial forests. Two smaller maxima are visible near 20°N , associated with high agricultural productivity in the Eastern US, and near 50°N due to strong vegetation activity in the forests of central Europe. For longitudes less than -25°E SIFTER shows a strong linear

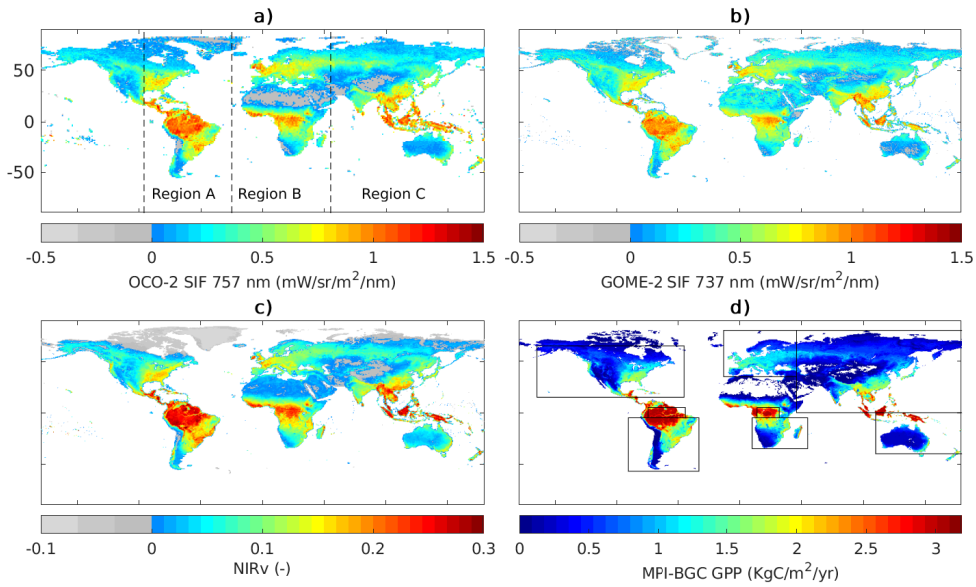


Figure 3.1: Global map of annual average SIF derived from (a) OCO-2 in $1^\circ \times 1^\circ$ grid cell, (b) SIFTER derived from GOME-2A in $0.5^\circ \times 0.5^\circ$ grid cell, (c) NIRv in $0.5^\circ \times 0.5^\circ$ grid cell in the years (2015-2018) and (d) GPP from the MPI-BGC $0.5^\circ \times 0.5^\circ$ grid cell in the years (2007-2011). The black dashed line in panel a) is to categorize the globe into three Continent-wise zones. The rectangular boxes in panel c) refers to regions used for spatial averages of SIF over continents and rain forest areas.

correlation with OCO-2 SIF ($R = 0.93$) and MPI-BGC GPP ($R = 0.92$).

Fig. 3.2 also shows higher productivity was observed over temperate ecosystems during July while it is during March over tropical regions. Particularly, all datasets show a global maximum vegetation productivity over US corn-belt during July which is even greater than the productivity of Amazon during its corresponding maximum productivity month of the equatorial rain forest regions (March). A notable discrepancy between GOME-2 SIFTER and OCO-2 SIF is observed over the tropical islands of Indonesia and the Philippines particularly during July, where SIFTER estimates a lower value compared to OCO-2. SIFTER shows a maximum zonal mean around 20°N while others show a maximum productivity around 0°N (see Fig. 3.2c). In the retrieval of GOME SIF over these small islands, there will be a large chance for the ocean values to be included in the larger pixel size of GOME-2 which possibly contribute for large uncertainty of SIF over densely populated with small islands. Moreover, in comparison to OCO-2 SIF, GOME-2 has a lower SIF value over tropical regions, especially in Indonesians in all season, also in Amazon and tropical rain forest of Africa during dry season. This is most likely due to contamination of SIF with cloud over the coarse resolution of GOME footprint data as compared to the more finer footprint of OCO-2 or due to strict cloud screening during the GOME-2 SIF retrieval which possibly decreases the number of samples included the gridded average. Köhler et al. [2015] noted a lower magnitude of GOME-2 SIF with increasing the cloud threshold. In contrast, higher value of SIF from GOME-2A as compared to OCO-2 SIF was observed over the Sahara desert which is systematically higher in March when the aerosol loading of the region is high than July. This is most likely resulted from the errors in the apparent reflectance caused by inaccurate aerosol characterization.

We see the patterns of Month-to-month variability of SIF and NIRv at a continental scale (see box in Fig 3.1d) covering the period from 2015-2018. In general, there is a high degree of correlation among the seasonal cycles

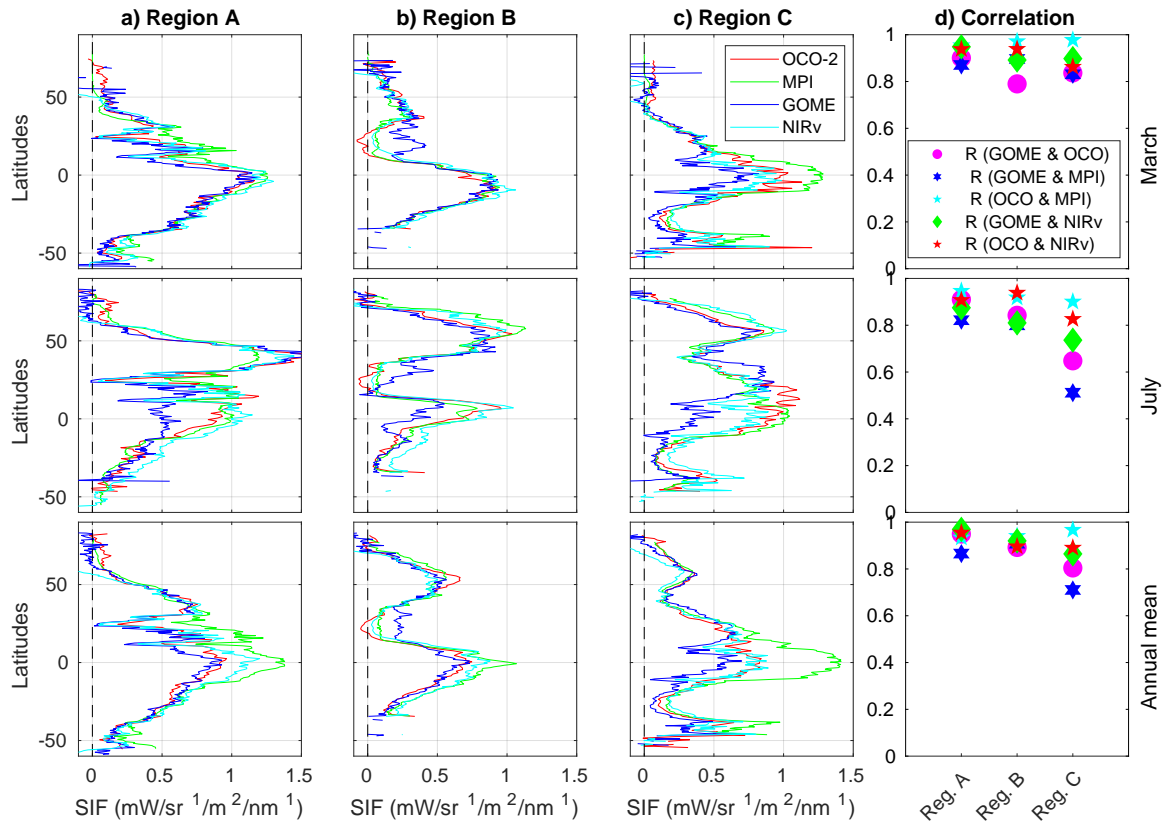


Figure 3.2: Continent wise zonal mean SIF from satellite sounding and GPP from Beer et al. [2010] during March (top) and July (middle) and annual mean (bottom) covering the years from 2015-2018 for North and South America (longitude from -96° to -25° E) a), Europe and Africa (longitude from -25° to 55° E) and b), Asia and Australia (longitude greater than 55° E) c) and corresponding correlation between datasets d). See Fig. 3.1a for the region categories.

of SIF observed by OCO-2, SIFTER and NIRv (Fig. 3.3). This correlation between datasets decreases over regions where there is no clear seasonality like in rain forest and vegetation-free areas. For the Amazonian rainforests, a gradual “green-up” from the early to end of the dry season (June to November) is observed in all four datasets, despite a somewhat stronger seasonal swing in GOME-2A SIF. This shows a notable discrepancy over the tropical rain forest regions of Amazon and also in Africa. In these tropical rain forest regions, GOME-2 SIFTER shows a clear seasonality with a double peak in SIFTER whereas OCO-2 SIF and NIRv hardly show such a double pick (See Fig. 3.3 Amazon and Tropical Africa). Particularly, in the Amazon forest, one of the peaks in SIF is observed during the dry months (September to October). Doughty et al. [2019] explained the chance of increasing GPP during the end of dry season following the loss of old-age leaves and the flushing of new leaves. In the African rain forest, SIFTER starts to decrease in April and reaches a minimum during the dry season in the boreal summer from June through August (See Fig. 3.3 Tropical Africa). The less good correlation in Australia is most likely due to the weak correlation of GOME-2 SIFTER and OCO-2 SIF over vegetation-free areas of the continent. Overall, slightly higher values of OCO-2 SIF are due to the difference in the measurement time as OCO-2 measures at maximum solar illumination.

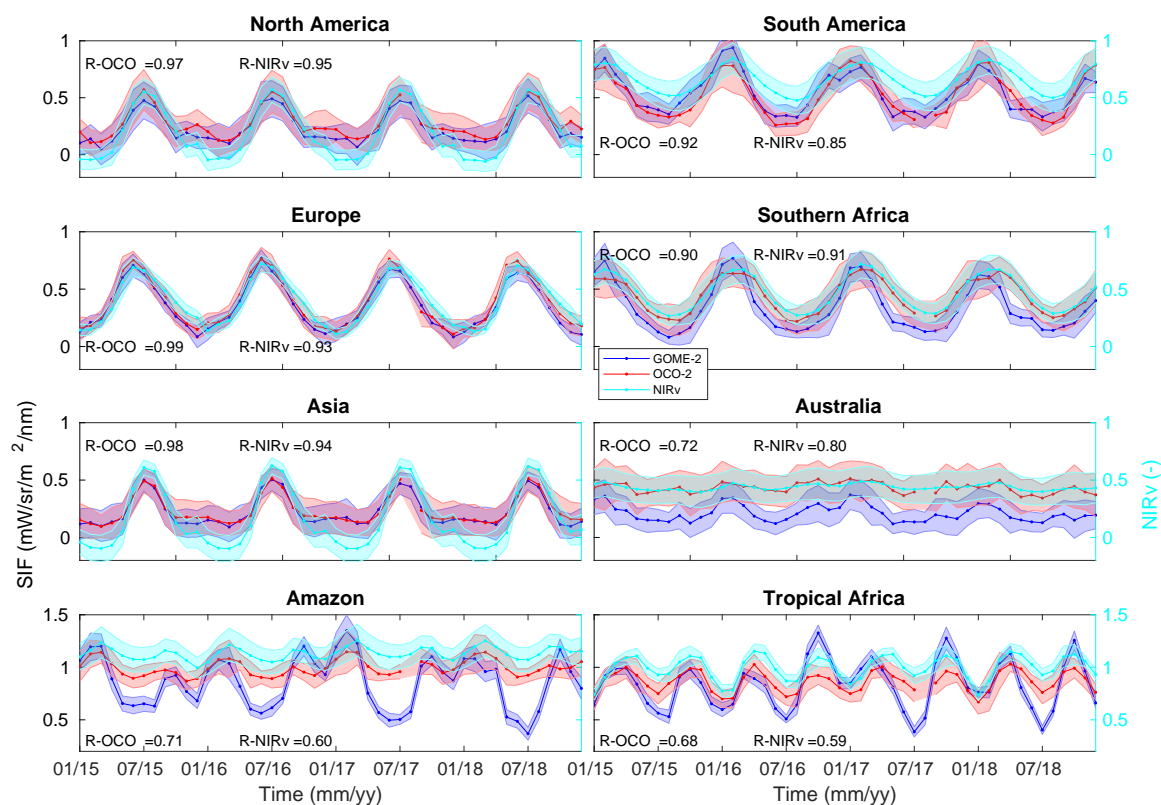


Figure 3.3: Monthly time series of SIF from GOME-2 SIFTER at 737 nm, OCO-2 SIF at 757 nm and NIRv in the years 2015-2018 over different regions across the globe. SIF and NIRv values are spatially averaged within the rectangle boxes shown in Fig. 3.1d. The coordinates of the regions are: North America (165-45 W and 15-65N), South America (91°-33°W and 57°-5°S), Europe (13°W-46°E and 35°-80°N), Southern Africa (10° - 55°E and 35°-5°S), Asia (46°-180°E and 0°-80°N), Australia (110°-180°E and 40°-0°S), Amazon (75°-44°W and 5°S - 5°N) and Tropical Africa (14° - 32°E and 5°S-5°N)

3.2 Inter-comparison at ecosystem level

An ecosystem level inter-comparison was performed around the five flux towers. The region we selected covers a $1^\circ \times 1^\circ$ window centering each flux towers. Fig. 3.4 depicts the level of agreement between GOME-2 SIFTER and OCO-2 SIF recalculated at 740 nm near the flux towers. Because of the difference in the overpass time of these two satellites, we allow a maximum time interval of 5 hours between their soundings. Then the time series obtained by this criteria covering the period from Sep 2014 to Dec 2018 was compared. The correlation between GOME-2 SIFTER and OCO-2 SIF ranges from strong (0.8) around the DE-RuS tower to weak (0.36) around the BR-Sa1 tower.

We also observe that the EC GPP at 13:30 hrs is slightly higher than the GPP at 9:30 hrs. For example, for US-MMS tower we found a mean difference of $0.8 \mu\text{molCO}_2\text{m}^{-2}\text{s}^{-1}$ higher GPP during the OCO-2 overpass time then the GOME-2 in the years 2007-2014. During the overpass time of OCO-2 (13:30 hr LT) the plant canopy is exposed to a higher intensity of irradiance, which possibly leads to a higher photosynthesis rate. In contrast, the relationship between plant physiology and photosynthesis shows plants are found to a higher rate of photosynthesis per amount of solar illumination during mid-morning. This may be the reason why GPP at this time has a slight difference. Solar radiation photosynthesis activity is affected by several environmental factors like temperature and water vapor pressure deficiency. These environmental factors have a strong diurnal

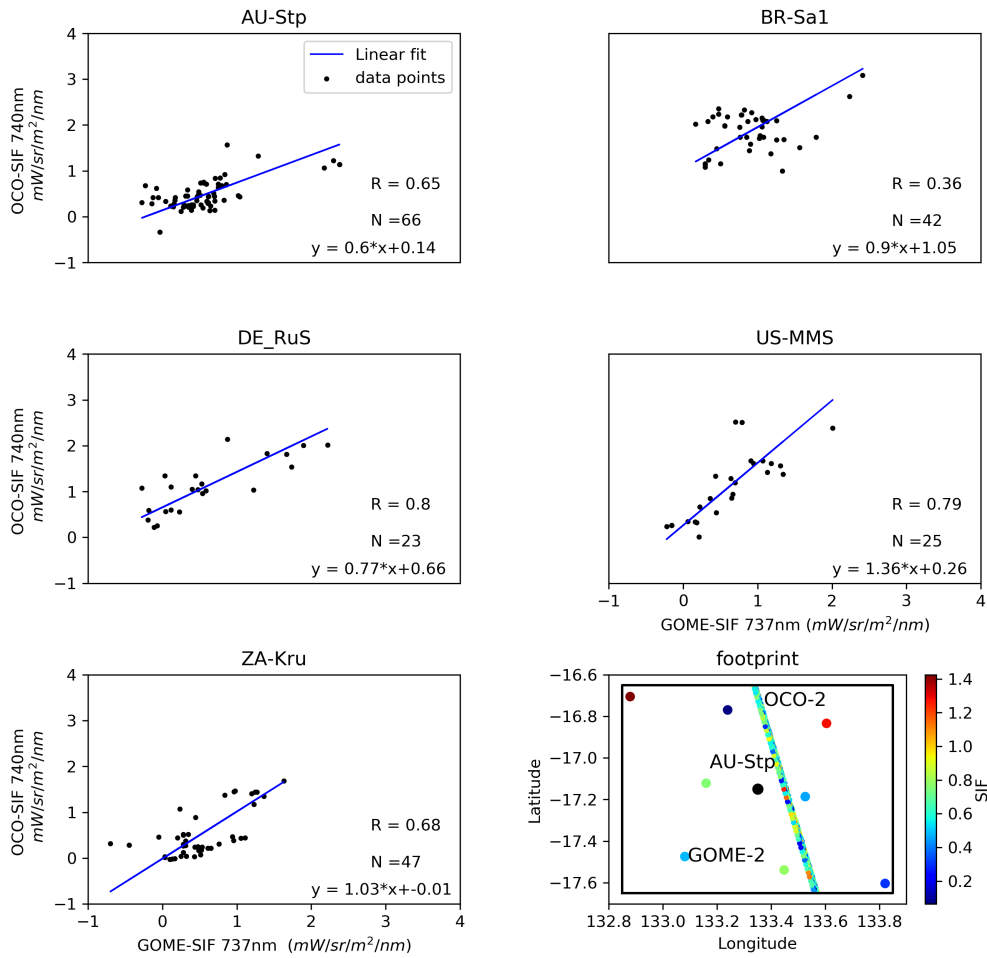


Figure 3.4: Scatter plot of OCO-2 SIF at 740 nm versus GOME-2 SIF at 737 nm near the flux towers covering the period from September 2014 to December 2018. The reduced Major axis regression (RMA) is used here for the fitting. (footprint) Spatial resolution of OCO-2 SIF 1.3 km by 2.25 km compared with products from GOME-2 (40 km by 40 km). footprint) shows coincident measurements of SIF from OCO-2 and GOME-2 sampled on January 30, 2015 overpasses around AU-Stp flux tower.

cycle. As a result, SIF also has a strong diurnal cycle, superimposed on the seasonal, spatial and interannual variations. The diurnal cycle of GPP was found to be approximately Gaussian with a maximum near midday. Zhang et al. [2018] shows that GPP and SIF are higher during the OCO-2 overpass time than GOME-2's overpass time. Zhang et al. [2018] also found less variation between the daily mean and instantaneous GPP during the maximum production hour of the day (from 8:00 to 16:00). Such difference will affect studies that aim to find an empirical equivalence between SIF and SIF-GPP from the two datasets. Our intercomparison study focuses more on their pattern than the empirical equivalence. Thereby, the difference in the numerical values will not bring any pronounced differences between the level of agreement in the two datasets. To test if there is a pattern similarity during the two overpass times, we calculate the correlation between EC

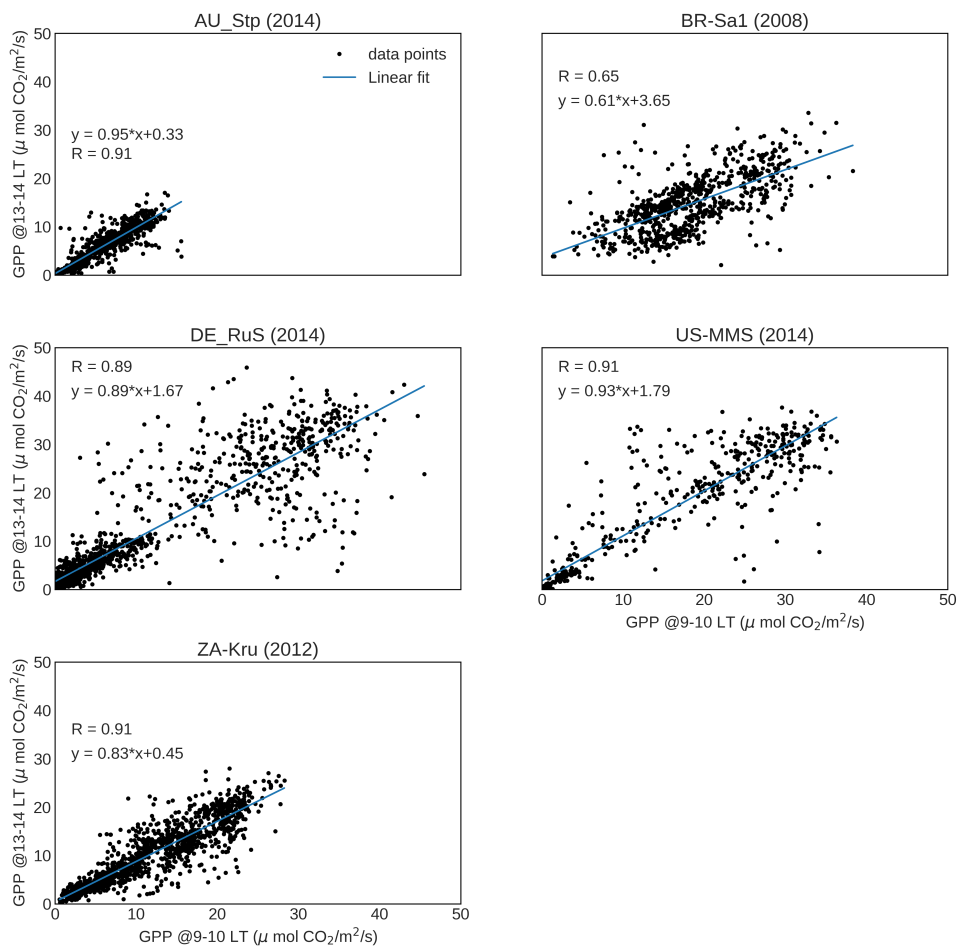


Figure 3.5: Comparison of EC GPP around the overpass time of OCO-2 (13:00 - 14:00 hrs LT) and GOME-2 (9:00 - 10:00 hrs LT) for the towers. All valid measurements from the year indicated in parents as a title for each site were considered in the comparison.

GPP from each tower, aggregated in time around the observation of GOME-2 (9:00-10:00 hrs) and the GPP product at local overpass time of OCO-2/GOSAT (13:00-14:00 hrs). To see the effect of this difference in the measurement time we correlate the tower GPP at the overpass time of OCO-2 versus GOME-2. We found an excellent agreement with a correlation coefficient higher than 0.9 for most of the flux towers, supporting our hypothesis that the difference in overpass time will not introduce considerable variation in the correlation between the satellite products (see Fig. 3.5).

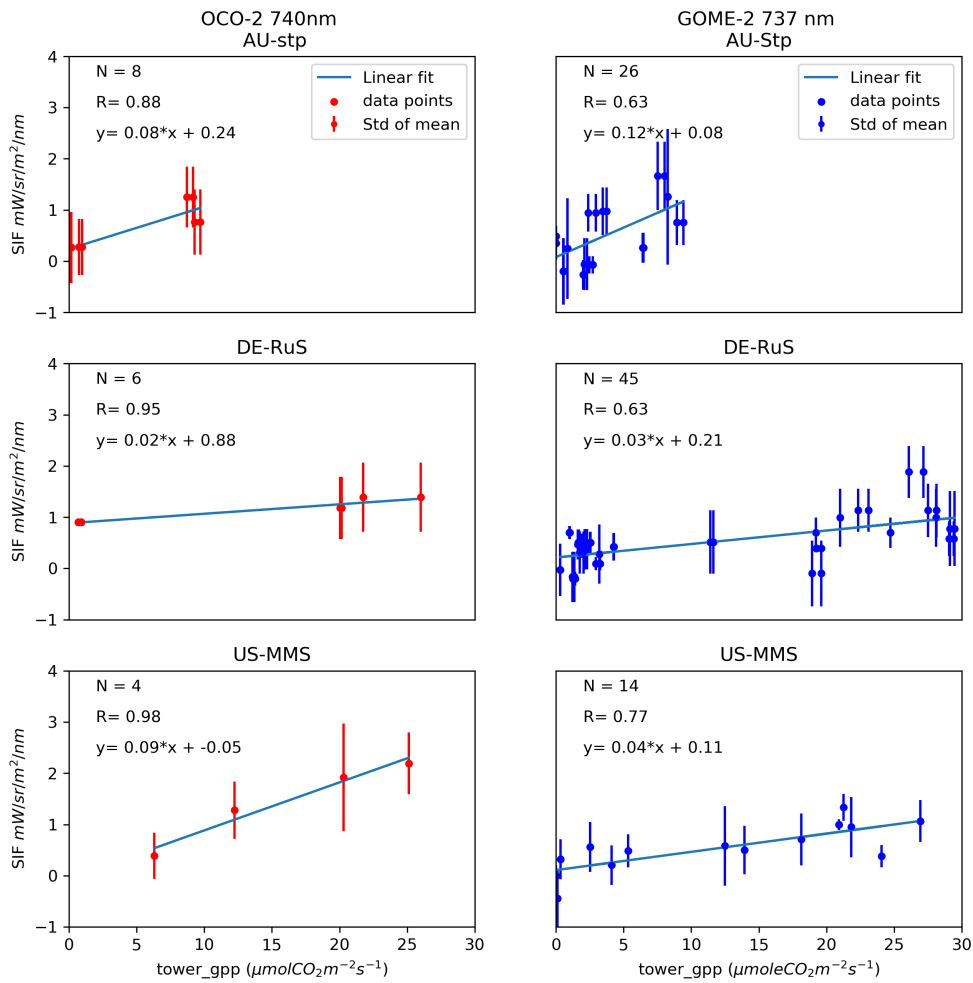


Figure 3.6: Scatter plot of SIF from OCO-2 (left) and GOME-2 (right) versus FLUXNET2015 GPP. Measurements are selected for a $1^\circ \times 1^\circ$ window centered around the tower, averaged for a time interval of 1 hour around the sensing time. Data points are covering the period from September to December 2014. The error bars refers to the standard deviation when calculating the mean.

3.3 Comparison of SIFTER with OCO-2 SIF and EC GPP

Fig. 3.6 shows a direct comparison of SIF from OCO-2 and GOME-2 with EC GPP during the overlap period of the three datasets, covering the period from September to December 2014. OCO-2 SIF shows a better correlation than GOME-2 over all the study sites. This is most likely due to a measurement scene of OCO-2 that is smaller than GOME-2A and thus more representative for the footprint of the flux tower measurement than GOME-2A which possibly results in a better correlation between OCO-2 SIF and EC GPP than SIFTER. Note that, due to few months of overlap with the eddy measurements, this comparison is made using only four months (September - December 2014) of overlap between the three datasets and the results may significantly

change when other months are included due to seasonal variations.

3.4 Comparison SIFTER with NIRv and EC GPP

Fig. 3.7 shows a monthly comparison of GOME-2 SIFTER and NIRv with EC GPP for these selected five towers at a coarse (0.5°) and high (0.05°) spatial resolution. Here, we use the ratio of NIRv at 0.5 to 0.05 degrees as a scale factor to create a SIFTER at 0.05 degrees. Using fine resolutions shows a significant improvement in relation to the EC GPP than the coarse resolution. The correlation SIFTER and NIRv were strong over the US-MMS where deciduous broad leaf forest dominates the region with a clear leaves up and down seasonality and moderate correlations over Brazil BR-Sa1 most likely due to the retrieval uncertainty over dark forests. Previous works also found that SIF has a strong correlation for agricultural regions and decreases over savanna and woodlands and becomes weak over evergreen forests [Guanter et al., 2014; Sanders et al., 2016]. Time series of SIFTER does not show the degradation problem which is observed in previous versions of SIFTER [Koren et al., 2018] likely due to a recent algorithm update. However, degradation still exists over the BR-Sa1 site.

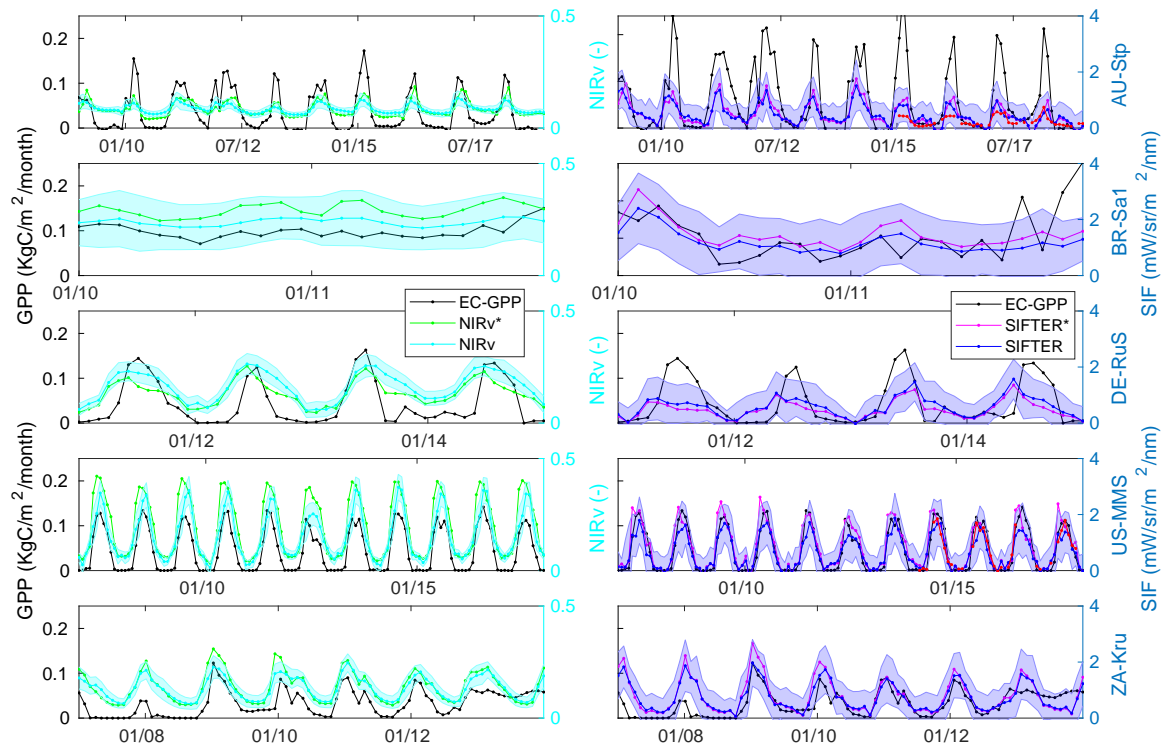


Figure 3.7: Time series comparison of monthly averaged coarse and fine resolution NIRv (left) and SIFTER (right) with available EC GPP. The red line in right shows time series OCO-2 SIF. The shaded region displays standard deviation of mean.

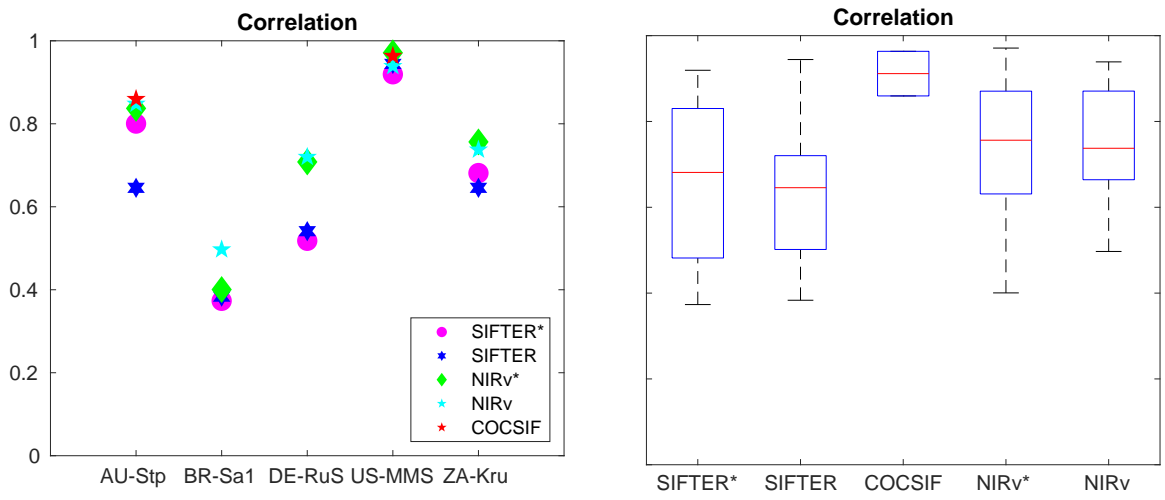


Figure 3.8: Temporal correlation of SIFTER*, SIFTER, OCO-2 SIF, NIRv* and NIRv with EC-GPP from the flux towers (left panel) and the boxplots of the correlation values for the relationships between these GPP proxies and EC-GPP of the towers at the monthly scale across these sites.

Chapter 4

Conclusions

We have tested the applicability of SIFTER in estimation primary production at global and ecosystem level by comparing these indices against field measurements from five sites across the globe. We compare the GOME-2A SIFTER v2 with NIRv and retrieval of SIF from OCO-2. We also investigated its relationship with GPP from the Max Planck institute of Biogeochemistry and EC GPP from five eddy covariance flux towers across the globe. Our results demonstrate that GOME-2A SIFTER v2 has a strong agreement in capturing the spatial distribution of SIF from OCO-2 and GPP from MPI-BGC. SIFTER v2 is well correlated with OCO-2 SIF, NIRv and MPI-BGC GPP in capturing seasonal cycles over continents and rain forest regions of Amazon and Africa. However, some discrepancies are observed over vegetation free areas and Oceania in their spatial distribution. The assessment of SIFTER at ecosystem level shows correlation that ranges from strong to weak with EC GPP, NIRv and OCO-2 SIF across the towers. We also found that SIFTER shows a very clear seasonality in the Amazon and Africa rain forest with a double peak. Down-scaled SIFTER shows improvement than the coarse resolution promising for efficient determination of primary production, and that a simple modeling approach, based solely on NIRv, can be utilized to give reliable estimates of GPP at similar ecosystems.

Acknowledgements

We acknowledge support from the European Organization for the Exploitation of Meteorological satellites (EUMETSAT), and the Royal Netherlands Meteorological Institute (KNMI). Eddy covariance data was obtained from the FluxNet, OZFlux and ICOS we thank the PI's of each tower for their contribution the sites. We also like to thank NASA for providing OCO-2 SIF data.

List of Tables

2.1	Some basic information on the satellites used for the study. *After July 2013, the GOME-2(a) swath is half the size, pixels are 40x40 km ² and repeat cycle is increased to 3 days.	4
2.2	Information on flux-tower sites. * indicates flux observations before 2007 are available from the towers but we didn't use them in this study.	6

List of Figures

2.1	The location and vegetation type of eddy covariance flux towers used in the study. The symbols stand for flux towers. The base map is the Moderate Resolution Imaging Spectroradiometer (MODIS) global land cover classification (MCD12C1), and the dominant land cover types include water, evergreen needle-leaf forests (ENF), evergreen broadleaf forests (EBF), deciduous needle-leaf forests (DNF), deciduous broadleaf forests (DBF), mixed forests (MF), closed shrublands (CSH), open shrublands (OSH), woody savannas (WSA), savannas (SAV), grasslands (GRA), permanent wet land (WET), croplands (CRO), urban and built-up (urban), and barren or sparsely vegetated (barren). The bottom panels show the vegetation type in a 1° x 1° grid surrounding the flux towers, indicated by black markers.	5
3.1	Global map of annual average SIF derived from (a) OCO-2 in 1° x 1° grid cell, (b) SIFTER derived from GOME-2A in 0.5° x 0.5° grid cell, (c) NIRv in 0.5° x 0.5° grid cell in the years (2015-2018) and (d) GPP from the MPI-BGC 0.5° x 0.5° grid cell in the years (2007-2011). The black dashed line in panel a) is to categorize the globe into three Continent-wise zones. The rectangular boxes in panel c) refers to regions used for spatial averages of SIF over continents and rain forest areas.	9
3.2	Continent wise zonal mean SIF from satellite sounding and GPP from Beer et al. [2010] duringg March (top) and July (middle) and annual mean (bottom) covering the years from 2015-2018 for North and South America (longitude from -96 ° to -25°E) a), Europe and Africa (longitude from -25° to 55°E) and b), Asia and Australia (longitude greater than 55°E) c) and corresponding correlation between datasets d). See Fig. 3.1a for the region categories.	10
3.3	Monthly time series of SIF from GOME-2 SIFTER at 737 nm, OCO-2 SIF at 757 nm and NIRv in the years 2015-2018 over different regions across the globe. SIF and NIRv values are spatially averaged within the rectangle boxes shown in Fig. 3.1d. The coordinates of the regions are: North America (165-45 W and 15-65N), South America (91°-33°W and 57°-5°S), Europe (13°W-46°E and 35°-80°N), Southern Africa (10° - 55°E and 35°-5°S), Asia (46°-180°E and 0°-80°N), Australia (110°-180°E and 40°-0°S), Amazon (75°-44°W and 5°S - 5°N) and Tropical Africa (14° - 32°E and 5°S-5°N)	11
3.4	Scatter plot of OCO-2 SIF at 740 nm verses GOME-2 SIFTER at 737 nm near the flux towers covering the period from September 2014 to December 2018. The reduced Major axis regression (RMA) is used here for the fitting. (footprint) Spatial resolution of OCO-2 SIF 1.3 km by 2.25 km compared with products from GOME-2 (40 km by 40 km). footprint) shows coincident measurements of SIF from OCO-2 and GOME-2 sampled on January 30, 2015 overpasses around AU-Stp flux tower.	12

3.5 Comparison of EC GPP around the overpass time of OCO-2 (13:00 - 14:00 hrs LT) and GOME-2 (9:00 - 10:00 hrs LT) for the towers. All valid measurements from the year indicated in parents as a title for each site were considered in the comparison. 13

3.6 Scatter plot of SIF from OCO-2 (left) and GOME-2 (right) versus FLUXNET2015 GPP. Measurements are selected for a 1° x 1° window centered around the tower, averaged for a time interval of 1 hour around the sensing time. Data points are covering the period from September to December 2014. The error bars refers to the standard deviation when calculating the mean. 14

3.7 Time series comparison of monthly averaged coarse ad fine resolution NIRv (left) and SIFTER (right) with available EC GPP. The red line in right shows time series OCO-2 SIF. The shaded region displays standard deviation of mean. 15

3.8 Temporal correlation of SIFTER*, SIFTER, OCO-2 SIF, NIRv* and NIRv with EC-GPP from the flux towers (left panel) and the boxplots of the correlation values for the relationships between these GPP proxies and EC-GPP of the towers at the monthly scale across these sites. 16

Bibliography

- Aubinet, M., Vesala, T., and Papale, D.: Eddy covariance: a practical guide to measurement and data analysis, Springer Science & Business Media, 2012.
- Badgley, G., Field, C. B., and Berry, J. A.: Canopy near-infrared reflectance and terrestrial photosynthesis, *Science advances*, 3, e1602 244, 2017.
- Baldocchi, D. D.: Assessing ecosystem carbon balance: problems and prospects of the eddy covariance technique, *Global Change Biol*, 9, 479–492, 2003.
- Beer, C., Reichstein, M., Tomelleri, E., Ciais, P., Jung, M., Carvalhais, N., Rödenbeck, C., Arain, M. A., Baldocchi, D., Bonan, G. B., et al.: Terrestrial gross carbon dioxide uptake: global distribution and covariation with climate, *Science*, 329, 834–838, 2010.
- Callies, J., Corpaccioli, E., Eisinger, M., Hahne, A., and Lefebvre, A.: GOME-2-Metop’s second-generation sensor for operational ozone monitoring, *ESA bulletin*, 102, 28–36, 2000.
- Carr, J. R.: Orthogonal regression: a teaching perspective, *International Journal of Mathematical Education in Science and Technology*, 43, 134–143, 2012.
- Clarke, M.: The reduced major axis of a bivariate sample, *Biometrika*, 67, 441–446, 1980.
- DAAC, O.: Oak Ridge National Laboratory Distributed Active Archive Center (ORNL DAAC), 2011.
- Doughty, R., Köhler, P., Frankenberg, C., Magney, T. S., Xiao, X., Qin, Y., Wu, X., and Moore, B.: TROPOMI reveals dry-season increase of solar-induced chlorophyll fluorescence in the Amazon forest, *Proceedings of the National Academy of Sciences*, 116, 22 393–22 398, 2019.
- Duveiller, G. and Cescatti, A.: Spatially downscaling sun-induced chlorophyll fluorescence leads to an improved temporal correlation with gross primary productivity, *Remote Sensing of Environment*, 182, 72–89, 2016.
- Frankenberg, C., Fisher, J. B., Worden, J., Badgley, G., Saatchi, S. S., Lee, J.-E., Toon, G. C., Butz, A., Jung, M., Kuze, A., et al.: New global observations of the terrestrial carbon cycle from GOSAT: Patterns of plant fluorescence with gross primary productivity, *Geophysical Research Letters*, 38, 2011.
- Friedman, J., Bohonak, A. J., and Levine, R. A.: When are two pieces better than one: fitting and testing OLS and RMA regressions, *Environmetrics*, 24, 306–316, 2013.
- Guanter, L., Zhang, Y., Jung, M., Joiner, J., Voigt, M., Berry, J. A., Frankenberg, C., Huete, A. R., Zarco-Tejada, P., Lee, J.-E., et al.: Global and time-resolved monitoring of crop photosynthesis with chlorophyll fluorescence, *Proceedings of the National Academy of Sciences*, 111, E1327–E1333, 2014.

- Guanter, L., Aben, I., Tol, P., Krijger, J., Hollstein, A., Köhler, P., Damm, A., Joiner, J., Frankenberg, C., and Landgraf, J.: Potential of the TROPOspheric Monitoring Instrument (TROPOMI) onboard the Sentinel-5 Precursor for the monitoring of terrestrial chlorophyll fluorescence, *Atmospheric Measurement Techniques*, 8, 1337–1352, 2015.
- ICOS: Drought 2018 Team and ICOS Ecosystem Thematic Centre: Drought-2018 ecosystem eddy covariance flux product in FLUXNET-Archive format - release 2019-1, <https://doi.org/10.18160/PZDK-EF78>, 2019.
- Isaac, P., Cleverly, J., McHugh, I., Van Gorsel, E., Ewenz, C., and Beringer, J.: OzFlux Data: Network integration from collection to curation, *Biogeosciences*, 2017.
- Joiner, J., Guanter, L., Lindstrot, R., Voigt, M., Vasilkov, A., Middleton, E., Huemmrich, K., Yoshida, Y., and Frankenberg, C.: Global monitoring of terrestrial chlorophyll fluorescence from moderate-spectral-resolution near-infrared satellite measurements: methodology, simulations, and application to GOME-2, *Atmospheric Measurement Techniques*, 6, 2803–2823, 2013.
- Joiner, J., Yoshida, Y., Guanter, L., and Middleton, E. M.: New methods for the retrieval of chlorophyll red fluorescence from hyperspectral satellite instruments: simulations and application to GOME-2 and SCIAMACHY, *Atmospheric Measurement Techniques*, 9, 2016.
- Jung, M., Reichstein, M., Margolis, H. A., Cescatti, A., Richardson, A. D., Arain, M. A., Arneth, A., Bernhofer, C., Bonal, D., Chen, J., et al.: Global patterns of land-atmosphere fluxes of carbon dioxide, latent heat, and sensible heat derived from eddy covariance, satellite, and meteorological observations, *Journal of Geophysical Research: Biogeosciences*, 116, 2011.
- Kilmer, J. and Rodríguez, R.: Ordinary least squares regression is indicated for studies of allometry, *Journal of evolutionary biology*, 30, 4–12, 2017.
- Köhler, P., Guanter, L., and Joiner, J.: A linear method for the retrieval of sun-induced chlorophyll fluorescence from GOME-2 and SCIAMACHY data. *Atmos Meas Tech* 8: 2589–2608, 2015.
- Koren, G., van Schaik, E., Araújo, A. C., Boersma, K. F., Gärtner, A., Killaars, L., Kooreman, M. L., Kruijt, B., van der Laan-Luijkx, I. T., von Randow, C., et al.: Widespread reduction in sun-induced fluorescence from the Amazon during the 2015/2016 El Niño, *Philosophical Transactions of the Royal Society B: Biological Sciences*, 373, 20170408, 2018.
- Li, X. and Xiao, J.: Mapping photosynthesis solely from solar-induced chlorophyll fluorescence: A global, fine-resolution dataset of gross primary production derived from OCO-2, *Remote Sensing*, 11, 2563, 2019.
- Liu, H., Feng, J., Järvi, L., and Vesala, T.: Four-year (2006–2009) eddy covariance measurements of CO₂ flux over an urban area in Beijing, *Atmospheric Chemistry and Physics*, 12, 7881–7892, 2012.
- Magney, T. S., Frankenberg, C., Köhler, P., North, G., Davis, T. S., Dold, C., Dutta, D., Fisher, J. B., Grossmann, K., Harrington, A., et al.: Disentangling changes in the spectral shape of chlorophyll fluorescence: Implications for remote sensing of photosynthesis, *Journal of Geophysical Research: Biogeosciences*, 2019.
- Munro, R., Eisinger, M., Anderson, C., Callies, J., Corpaccioli, E., Lang, R., Lefebvre, A., Livschitz, Y., and Albinana, A. P.: GOME-2 on MetOp, in: *Proc. of The 2006 EUMETSAT Meteorological Satellite Conference*, Helsinki, Finland, vol. 1216, p. 48, 2006.
- Quéré, C. L., Moriarty, R., Andrew, R., Canadell, J., Sitch, S., Korsbakken, J., Friedlingstein, P., Peters, G., Andres, R., Boden, T., et al.: Global carbon budget 2015, *Earth System Science Data*, 7, 349–396, 2015.

- Sanders, A., Verstraeten, W., Kooreman, M., Van Leth, T., Beringer, J., and Joiner, J.: Spaceborne sun-induced vegetation fluorescence time series from 2007 to 2015 evaluated with Australian flux tower measurements, *Remote Sensing*, 8, 895, 2016.
- Schaaf, C. and Wang, Z.: MCD43C4 MODIS/Terra+Aqua BRDF/Albedo Nadir BRDF-Adjusted Ref Daily L3 Global 0.05Deg CMG V006 [Data set]. NASA EOSDIS Land Processes DAAC. Accessed 2019-02-12, <https://doi.org/10.5067/MODIS/MCD43C4.006>, 2015.
- Schlau-Cohen, G. S. and Berry, J.: Photosynthetic fluorescence, from molecule to planet, *Physics Today*, 68, 2015.
- Sims, D. A., Rahman, A. F., Cordova, V. D., Baldocchi, D. D., Flanagan, L. B., Goldstein, A. H., Hollinger, D. Y., Misson, L., Monson, R. K., Schmid, H. P., et al.: Midday values of gross CO₂ flux and light use efficiency during satellite overpasses can be used to directly estimate eight-day mean flux, *Agricultural and Forest Meteorology*, 131, 1–12, 2005.
- van Schaik, E., Kooreman, M. L., Stammes, P., Tilstra, L. G., Tuinder, O. N. E., Sanders, A. F. J., Verstraeten, W. W., Lang, R., Cacciari, A., Joiner, J., Peters, W., and Boersma, K. F.: Improved SIFTER v2 algorithm for long-term GOME-2A satellite retrievals of fluorescence with a correction for instrument degradation, *Atmospheric Measurement Techniques Discussions*, 2020, 1–33, <https://doi.org/10.5194/amt-2019-384>, URL <https://www.atmos-meas-tech-discuss.net/amt-2019-384/>, 2020.
- Wei, X., Wang, X., Wei, W., and Wan, W.: Use of sun-induced chlorophyll fluorescence obtained by OCO-2 and GOME-2 for GPP estimates of the Heihe River basin, China, *Remote Sensing*, 10, 2039, 2018.
- Zeng, Y., Badgley, G., Dechant, B., Ryu, Y., Chen, M., and Berry, J. A.: A practical approach for estimating the escape ratio of near-infrared solar-induced chlorophyll fluorescence, *Remote Sensing of Environment*, 232, 111 209, 2019.
- Zhang, Y., Xiao, X., Zhang, Y., Wolf, S., Zhou, S., Joiner, J., Guanter, L., Verma, M., Sun, Y., Yang, X., et al.: On the relationship between sub-daily instantaneous and daily total gross primary production: Implications for interpreting satellite-based SIF retrievals, *Remote sensing of environment*, 205, 276–289, 2018.